

## Design of high-speed MUTC-PD with electric field regulation layer

XU Jian-bo, LIU Kai, DONG Xiao-wen, DUAN Xiao-feng, HUANG Yong-qing, WANG Qi, REN Xiao-min

### Citation:

XU Jian-bo, LIU Kai, DONG Xiao-wen, DUAN Xiao-feng, HUANG Yong-qing, WANG Qi, REN Xiao-min. Design of high-speed MUTC-PD with electric field regulation layer[J]. *Chinese Optics*, 2025, 18(2): 393-400. doi: 10.37188/CO.EN-2024-0030  
徐建波, 刘凯, 董晓雯, 段晓峰, 黄永清, 王琦, 任晓敏. 具有电场调控层的高速MUTC-PD设计[J]. *中国光学*, 2025, 18(2): 393-400. doi: 10.37188/CO.EN-2024-0030

View online: <https://doi.org/10.37188/CO.EN-2024-0030>

## Articles you may be interested in

### Research progress of high-speed vertical-cavity surface-emitting laser in CIOMP

长春光机所高速垂直腔面发射激光器研究进展

*Chinese Optics*. 2022, 15(5): 946 <https://doi.org/10.37188/CO.2022-0136>

### Principle and application of metasurface optical field modulation of atomic layer thickness

原子层厚度超表面光场调控原理及应用

*Chinese Optics*. 2021, 14(4): 851 <https://doi.org/10.37188/CO.2021-0069>

### A study on the epitaxial structure and characteristics of high-efficiency blue silicon photodetectors

高效率蓝光硅光探测器外延结构及特性研究

*Chinese Optics*. 2022, 15(3): 568 <https://doi.org/10.37188/CO.2021-0188>

### Design of a 20 m underwater wireless optical communication system based on blue LED

20 m水下无线蓝光LED通信系统样机设计

*Chinese Optics*. 2021, 14(6): 1451 <https://doi.org/10.37188/CO.2020-0190>

### Integrated Nitride optoelectronic chip for motion detection and visible light communication

运动探测及可见光通信一体化氮化物光电子芯片

*Chinese Optics*. 2023, 16(5): 1257 <https://doi.org/10.37188/CO.2023-0028>

### Analysis of photoelectric characteristics of a light-damaged schottky perovskite detector

光损伤肖特基钙钛矿探测器的光电特性分析

*Chinese Optics*. 2022, 15(4): 668 <https://doi.org/10.37188/CO.2021-0196>

文章编号 2097-1842(2025)02-0393-08

## Design of high-speed MUTC-PD with electric field regulation layer

XU Jian-bo<sup>1,2</sup>, LIU Kai<sup>1,2\*</sup>, DONG Xiao-wen<sup>1,2</sup>, DUAN Xiao-feng<sup>1,2</sup>,  
HUANG Yong-qing<sup>1,2</sup>, WANG Qi<sup>1,2</sup>, REN Xiao-min<sup>1,2</sup>

(1. State Key Laboratory of Information Photonics and Optical Communications, Beijing University of Posts and Telecommunications, Beijing 100876, China;

2. School of Electrical Engineering, Beijing University of Posts and Telecommunications, Beijing 100876, China)

\* Corresponding author, E-mail: kliu@bupt.edu.cn

**Abstract:** This paper proposes a novel modified uni-traveling-carrier photodiode (MUTC-PD) featuring an electric field regulation layer: a p-type doped thin layer inserted behind the PD's n-doped cliff layer. This electric field regulation layer enhances the PD's performance by not only reducing and smoothing the electric field intensity in the collector layer, allowing photo-generated electrons to transit at peak drift velocity, but also improving the electric field intensity in the depleted absorber layer and optimizing the photo-generated carriers' saturated transit performance. Additionally, the transport characteristics of the peak drift velocity of photogenerated electrons in the device's collection layer can be used to optimize its parasitic characteristics. The electron's peak drift velocity compensates for the lost transit time. Thus improving the 3 dB bandwidth of the PD's photo response. Finally obtains a MUTC-PD with a 3 dB bandwidth of 68 GHz at a responsivity of 0.502 A/W, making it suitable for 100 Gbit/s optical receivers.

**Key words:** peak electron drift velocity; transit performance; MUTC-PD; optical fiber communication; optical interconnect

## 具有电场调控层的高速 MUTC-PD 设计

徐建波<sup>1,2</sup>, 刘凯<sup>1,2\*</sup>, 董晓雯<sup>1,2</sup>, 段晓峰<sup>1,2</sup>, 黄永清<sup>1,2</sup>, 王琦<sup>1,2</sup>, 任晓敏<sup>1,2</sup>

(1. 北京邮电大学信息光子学与光通信全国重点实验室, 北京 100876;

2. 北京邮电大学电子工程学院, 北京 100876)

**摘要:** 本文提出了一种具有电场调控层的新型改进型单行载流子光探测器(MUTC-PD)。该光探测器中, 崖层后新增的

收稿日期: 2024-09-26; 修订日期: 2024-11-05

基金项目: 国家自然科学基金(No. 62374020); 淄博市科技型中小企业创新能力提升项目(No. 2022TSGC0046); 山东省科技型中小企业创新能力提升项目(No. 2022TSGC2290)

Supported by National Natural Science Foundation of China (No. 62374020); Zibo Science and Technology SMEs Innovation Capacity Improvement Project (No. 2022TSGC0046); Shandong Provincial Science and Technology SMEs Innovation Capacity Improvement Project (No. 2022TSGC2290)

p 型掺杂电场调控层能够优化收集层中的电场强度,从而使光生电子在收集层中以峰值漂移速度输运,同时能够增强耗尽吸收层中的电场强度,优化其中光生载流子饱和速度输运特性。此外,器件收集层中光生电子的峰值漂移速度输运特性可以进一步优化其寄生电容特性,从而显著提升光探测器的 3 dB 响应带宽。经过仿真优化设计,获得了响应度为 0.502 A/W, 3-dB 带宽为 68 GHz 的 MUTC-PD,可应用于 100 Gbit/s 光接收机。

**关键词:** 电子峰值速度; 输运特性; 改进型单行载流子光探测器; 光纤通信; 光互连

**中图分类号:** TN215      **文献标志码:** A      **doi:** 10.37188/CO.EN-2024-0030      **CSTR:** 32171.14.CO.EN-2024-0030

## 1 Introduction

To meet the exponentially growing demand for data traffic capacity in data centers, photodetectors must quickly respond to 100 Gbps signals with high sensitivity. Nowadays, a port transmission rate of 400 Gb/s is being scaled up in data centers. Transceiver modules with 800 Gb/s port rate are now undergoing small-scale trials, and those with 1.6 Tb/s port rate have entered the prototype stage. Corresponding port rate standards include 8×200 Gb/s, 8×100 Gb/s, etc., with different modulation schemes. This necessitates the development of high-speed photodetectors capable of supporting these standards, with their photo-response bandwidth exceeding 57 GHz and responsivity over 0.5 A/W, for applications in single-wavelength 100 Gb/s optical channels<sup>[1]</sup>. To accomplish the required PD performance, many attempts have been conducted, such as mushroom-type photodetectors<sup>[2]</sup>, dual-absorption-layer photodetectors<sup>[3]</sup>, PIN photodetectors<sup>[4]</sup>, PDA-PDs<sup>[5]</sup>, and uni-traveling-carrier photodiode (UTC-PD)<sup>[6]</sup>, etc. The UTC-PD, first proposed in 1997, effectively mitigates the space-charge effect in PIN PD by using electrons as a single transit carrier to promote its high-speed performance<sup>[6]</sup>. MUTC-PD optimizes the UTC-PD's absorber layer by dividing it into a p-doped region and a depleted region to obtain high speed and high responsivity performance simultaneously<sup>[7-8]</sup>. However, MUTC-PD typically features thin absorber layers for enhanced high-speed performance, resulting in lower responsivity. Increasing the thickness of the absorber layer allows a greater responsivity, but it increases the carrier's transit time and decreases the PD's bandwidth.

One possible method to reduce the PD's response bandwidth degradation caused by the thick absorption layer is to increase the mean electron transit velocity<sup>[9-11]</sup>.

In this paper, a novel MUTC-PD structure with an electric field regulation layer inserted between its cliff and collector layers is proposed for performance optimization. By optimizing the doping concentration of the electric field regulation layer and the thickness of the collector layer, the electric field intensity inside the MUTC-PD's collector layer can be tuned to a certain level to make the photo-generated electrons transit at their peak drift velocities constantly. At the same time, the electric field intensity in the PD's absorber could be optimized to ensure that the photo-generated hole would transit at its saturated drift velocity in its depleted region, and the photo-generated electron's diffusion enhancement factor could be maximized in its p-doped region. Moreover, as in the proposed novel MUTC-PD, the electrons transit at their peak drift velocity in the PD's collector layer, enabling further optimization of the PD's parasitic capacitance. This and the overall impact on the PD's high-speed photo-response were analyzed. In the analysis, for better coupling of the incident light, the diameter of the PD was set to 16 μm. The following sections of this paper will refer to the proposed MUTC-PD as the swift-responding modified uni-traveling-carrier photodiode (SMUTC-PD) to distinguish it from the MUTC-PD.

## 2 SMUTC-PD design

**Fig. 1** (color online) outlines the epitaxial structure of the SMUTC-PD. A 500 nm thick InP

buffer layer, with an n-doping level of  $5 \times 10^{18} \text{ cm}^{-3}$ , was deposited above the SI-InP substrate. On top of this, an un-intentionally doped InP collector layer with a thickness of  $x \text{ nm}$  was added to enable further optimization. A 20 nm thick InP electric field regulation layer with a p-doping level of  $1 \times 10^{16} \text{ cm}^{-3}$  was placed above the collector layer. This regulation layer was designed to regulate the electric field intensity distribution in the collector layer. Next, an 80 nm thick InP cliff layer with a n-doping level of  $7.2 \times 10^{16} \text{ cm}^{-3}$ , a 40 nm thick InGaAsP layer (Q1.24) with a p-doping level of  $5 \times 10^{15} \text{ cm}^{-3}$ , and a 40 nm thick InGaAsP layer (Q1.46) with a p-doping level of  $5 \times 10^{15} \text{ cm}^{-3}$  were added one by one consecutively. Q1.24 and Q1.46 represent the cut-off wavelengths of the corresponding InGaAsP materials. Then, a 100 nm thick, un-intentionally P-doped InGaAs layer and a 350 nm thick p-doped InGaAs layer with a doping level of  $3.5 \times 10^{16} \text{ cm}^{-3}$  were grown as absorption regions of the PD. Above it, a 50 nm thick InGaAsP electron block layer with a p-doping level of  $1 \times 10^{19} \text{ cm}^{-3}$  was grown. The top-most cap layer was a 50 nm thick p-doped InGaAs layer with a doping level of  $1 \times 10^{19} \text{ cm}^{-3}$ .

p-InGaAs $1 \times 10^{19} \text{ cm}^{-3}$ 50 nm
p-InGaAsP $1 \times 10^{19} \text{ cm}^{-3}$ 50 nm (Q1.12)
p-InGaAs $3.5 \times 10^{16} \text{ cm}^{-3}$ 350 nm
p-InGaAs $1 \times 10^{15} \text{ cm}^{-3}$ 100 nm
p-InGaAsP $5 \times 10^{15} \text{ cm}^{-3}$ 40 nm (Q1.46)
p-InGaAsP $5 \times 10^{15} \text{ cm}^{-3}$ 40 nm (Q1.24)
n-InP $7.2 \times 10^{16} \text{ cm}^{-3}$ 80 nm
p-InP $1 \times 10^{16} \text{ cm}^{-3}$ 20 nm
n-InP $1 \times 10^{15} \text{ cm}^{-3}$ $x \text{ nm}$
n-InP $5 \times 10^{18} \text{ cm}^{-3}$ 500 nm
n-InP Substrate 500 nm

Fig. 1 Epitaxial layer scheme

SMUTC-PD's performance simulations were conducted with Silvaco Atlas. An extra  $15 \Omega$  series resistance was added to the ideal  $50 \Omega$  load resistance to analyze its parasitic performance. Also, an additional parallel parasitic capacitance of  $5 \text{ fF}$  was added to simulate the capacitance introduced by the

metal contact pad. The negative differential mobility model was used to analyze the electron's peak drift velocity performance in InP. The bias voltage in the simulation was set to  $3 \text{ V}$ . The material parameters of InP, InGaAsP, and InGaAs were obtained from Ref. [12-15]. Table 1 gives the optical and electrical parameters of the materials used in the simulation (InP and InGaAs).

Tab. 1 Material parameters of the simulation

Parameter	InP	InGaAs
Electron mobility, $\mu_n$	$5400 \text{ cm}^2/\text{Vs}$	$12000 \text{ cm}^2/\text{Vs}$
Hole mobility, $\mu_p$	$200 \text{ cm}^2/\text{Vs}$	$300 \text{ cm}^2/\text{Vs}$
Conduction band density of states, $N_c$	$1.1 \times 10^{19} \text{ cm}^{-3}$	$7.7 \times 10^{18} \text{ cm}^{-3}$
Valence band density of states, $N_v$	$5.7 \times 10^{17} \text{ cm}^{-3}$	$2.1 \times 10^{17} \text{ cm}^{-3}$
Electron saturation velocity	$2.6 \times 10^7 \text{ cm/s}$	$2.5 \times 10^7 \text{ cm/s}$
Hole saturation velocity	$5 \times 10^6 \text{ cm/s}$	$5 \times 10^6 \text{ cm/s}$
Electron and hole lifetime	$2 \times 10^{-9} \text{ s}$	$1 \times 10^{-7} \text{ s}$
Electron auger coefficient	$3.7 \times 10^{-31} \text{ cm}^6/\text{s}$	$3.2 \times 10^{-28} \text{ cm}^6/\text{s}$
Hole auger coefficient	$8.7 \times 10^{-30} \text{ cm}^6/\text{s}$	$3.2 \times 10^{-28} \text{ cm}^6/\text{s}$
Real refractive index	3.2	3.51
Imaginary refractive index	0	0.106

As stated above, the SMUTC-PD introduces an electric field regulation layer (EFRL) to optimize the transit performance of the photo-generated electrons and holes. The transit bandwidth of SMUTC-PD was determined by the electron's transit time in the collector layer, the p-doped absorption layer, and the hole's transit time in the depleted absorption layer. The doping level of the EFRL was used to optimize the above parameters by adjusting the electric field intensity distribution in the three layers mentioned above. The simulation results are shown in Fig. 2 (color online). Electron and hole transit velocity distributions in the SMUTC-PD with different doping-level in EFRL are shown in Fig. 3–Fig. 4 (color online). In the above analysis, the thickness of the collector layer was set to  $900 \text{ nm}$ . Fig. 2 shows that the introduction of the EFRL made the electric field intensity distribution in the collector layer consistent. Thus, the electrons can transit

with uniform velocity throughout the collector layer. Moreover, the optimization of the electric field intensity distribution in the collector layer and the depleted absorption region was achieved by adjusting the doping of the EFRL, which was set to  $D_0$ . Reducing the value of  $D_0$  lowered the electric intensity in the collector layer (as shown in Fig. 2). The adjustment allowed the intensity to approach a level that enabled the electrons to transit through it at peak electron drift velocity, as shown in Fig. 3. At the same time, the electric intensity in the depleted absorption layer increased (as shown in Fig. 2), which enabled the holes' transit velocity to approach maximum level (the saturated hole drift velocity), as

shown in Fig. 4.

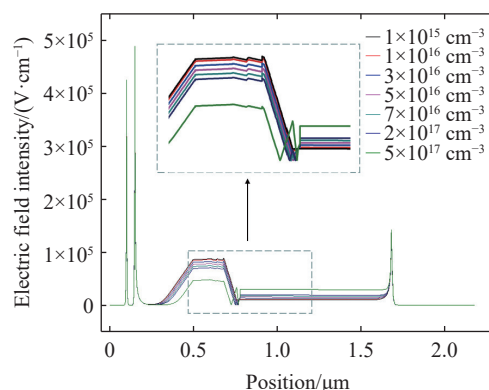


Fig. 2 SMUTC-PD's electric field intensity distribution at different doping concentrations in the electric field regulation layer

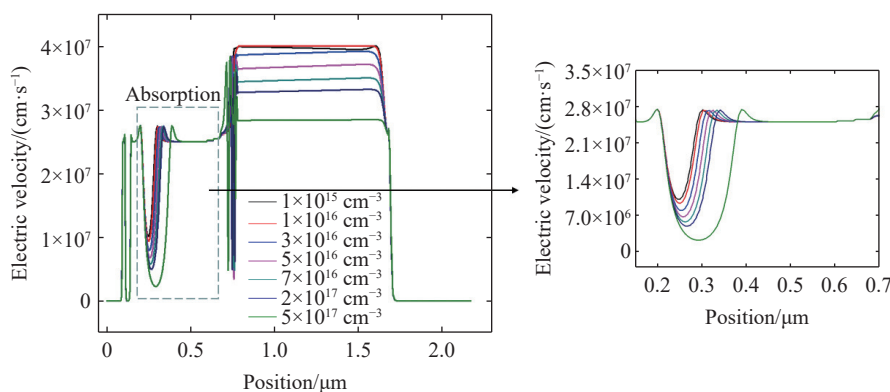


Fig. 3 SMUTC-PD's electron velocity distributions at different doping concentrations in the electric field regulation layer

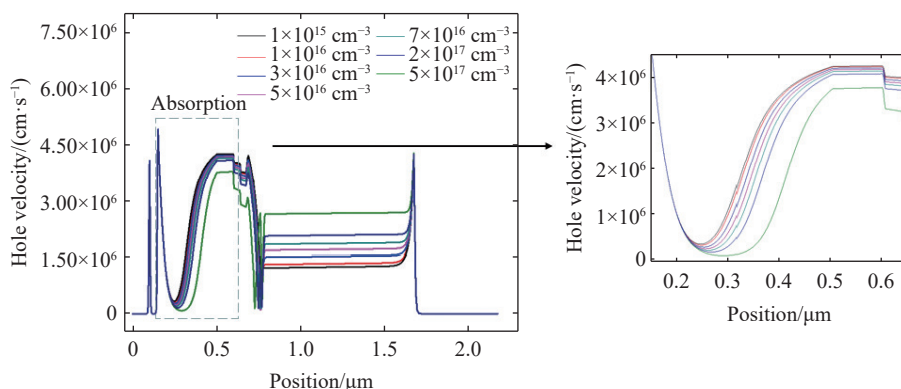


Fig. 4 SMUTC-PD's hole velocity distributions at different doping concentrations in the electric field regulation layer

As shown in Fig. 2, the electric field intensity in the collector layer rises from 13 kV/cm to 30 kV/cm when  $D_0$  goes from  $3 \times 10^{16} \text{ cm}^{-3}$  to  $5 \times 10^{17} \text{ cm}^{-3}$ . Specifically, the electric field intensity in the collector layer is approximated at 11 kV/cm when  $D_0$  is  $1 \times 10^{15} \text{ cm}^{-3}$  and  $1 \times 10^{16} \text{ cm}^{-3}$ . In this range, the electrons can transit in InP at its peak

drift velocity of  $4 \times 10^7 \text{ cm/s}$ . This was verified by the simulation analysis of the electron's transit velocity distribution in the SMUTC-PD, shown in Fig. 3. Furthermore, when  $D_0$  goes from  $3 \times 10^{16} \text{ cm}^{-3}$  to  $5 \times 10^{17} \text{ cm}^{-3}$ , the mean velocity of electrons in the collector layer decreases from  $3.8 \times 10^7 \text{ cm/s}$  to  $2.8 \times 10^7 \text{ cm/s}$ .

As Fig. 2 shows, when  $D_0$  is  $1 \times 10^{15} \text{ cm}^{-3}$  and  $1 \times 10^{16} \text{ cm}^{-3}$ , in the depleted absorption region, the electric field intensity is approximated to be 86 kV/cm, and the velocity of holes is  $4.3 \times 10^6 \text{ cm/s}$  as Fig. 4 shows, approaching its saturated drift velocity. From Fig. 2 and 4, one can see that the electric field intensity decreases from 85 kV/cm to 47 kV/cm when  $D_0$  goes from  $3 \times 10^{16} \text{ cm}^{-3}$  to  $5 \times 10^{17} \text{ cm}^{-3}$ , and the maximum velocity of holes decreases from  $4.2 \times 10^6 \text{ cm/s}$  to  $3.7 \times 10^6 \text{ cm/s}$ . Simultaneously, the electrons consistently transit at their saturation drift velocity of  $2.5 \times 10^7 \text{ cm/s}$ .

In the p-doped absorption region, the hole relaxes. When  $D_0$  is  $1 \times 10^{15} \text{ cm}^{-3}$  and  $1 \times 10^{16} \text{ cm}^{-3}$ , the minimum velocity of electrons is  $1.0 \times 10^7 \text{ cm/s}$  and  $9.3 \times 10^6 \text{ cm/s}$ , according to Fig. 3. When  $D_0$  goes from  $3 \times 10^{16} \text{ cm}^{-3}$  to  $5 \times 10^{17} \text{ cm}^{-3}$ , the minimum velocity of electrons decreases from  $7.9 \times 10^6 \text{ cm/s}$  to  $2.2 \times 10^6 \text{ cm/s}$ .

In summary, in the above three layers, when  $D_0$  is  $1 \times 10^{15} \text{ cm}^{-3}$  and  $1 \times 10^{16} \text{ cm}^{-3}$ , the transit performance of electrons and holes can be optimized. Ultimately, the doping concentration of  $1 \times 10^{16} \text{ cm}^{-3}$  was chosen for the EFRL layer, as in the above three layers. The collector layer is longer and has a greater impact on the PD's high-speed characteristics.

### 3 SMUTC-PD performance analysis

When optimizing the SMUTC-PD's dynamic photo-response performance, its collector layer's thickness is a major influencing factor. It determines most of the photo-generated electrons' transit time and the PD's junction capacitance. Therefore, the thickness of the PD's collector layer and its internal electric field intensity distribution need to be carefully designed. To improve the PD's dynamic performance, its collector's thickness can be increased to reduce its parasitic capacitance. At the same time, by optimizing the electric field intensity distribution in the PD's collector, as stated in section 2, the photo-generated electrons can transit

through the PD's collector at peak drift velocity. Then, the electron's transit time increase in the collector can be compensated for.

In the SMUTC-PD optimization, the PD collector's thickness  $x$  changed from 0.1  $\mu\text{m}$  to 1.3  $\mu\text{m}$ . And the PD's photo-response bandwidth was calculated correspondingly. Fig. 5–7 (color online) denotes the simulated PD's carrier transit time determined photo-response bandwidth as "Tt" and a solid blue line with square marks. At the same time, Fig. 5–7 denotes the parasitic capacitance simulated from SMUTC-PD structure as "capacitance" and a solid red line with triangle marks. Fig. 5–7 denotes the total PD's photo-response bandwidth that resulted from the carriers' transit time and the PD's parasitic effect in the simulation as "3 dB" and a solid green line with circle marks. As shown in Fig. 5, at the 3 V reverse bias voltage, in the collector's thickness  $x$  changing range, the transit time determined bandwidth of the PD decreases continuously from 109 GHz to 77 GHz, but the total bandwidth rises to a peak of 68 GHz at  $x=0.9 \mu\text{m}$ , then decreases. Therefore, the collector layer thickness was optimized at 900 nm. As stated in Section 2, the doping concentration of the EFRL affects the electric field intensity distribution in the collector layer and determines its mean electron transit velocity. In the simulations shown in Fig. 5, the mean electron transit velocity is optimized to its peak drift velocity.

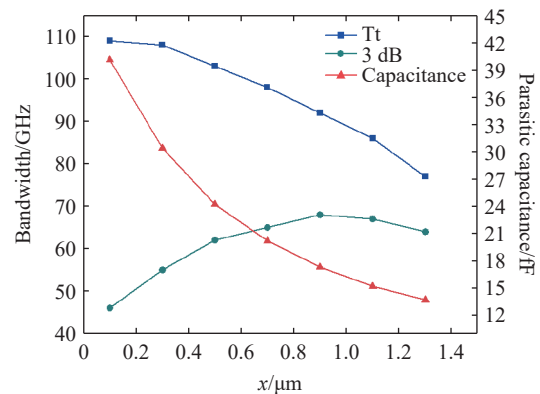


Fig. 5 SMUTC-PD's frequency response and parasitic capacitance with different collector layer thicknesses

In order to investigate the effect of the doping concentration and thickness of the p-doped absorption region on the SMUTC-PD's photo-response bandwidth, its doping concentration was set to change from  $3 \times 10^{16} \text{ cm}^{-3}$  to  $7 \times 10^{16} \text{ cm}^{-3}$  for short enough hole relaxation time. Its thickness is denoted as  $m \text{ }\mu\text{m}$ . Then, the thickness of the depleted absorption region was set to  $(0.45-m) \text{ }\mu\text{m}$ . The SMUTC-PD's frequency photo-response performance was simulated to determine the optimal doping concentration in the p-doped absorption region<sup>[16]</sup>. Fig. 6 shows the simulation results for the p-doped absorption region across various doping levels, while Fig. 7 shows the results for different  $m$  values. The optimal doping level for the p-doped absorption region was determined to be  $3.5 \times 10^{16} \text{ cm}^{-3}$ , while its optimal thickness was determined to be  $0.35 \text{ }\mu\text{m}$ .

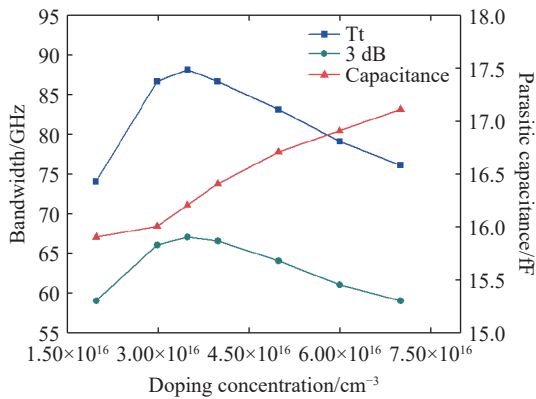


Fig. 6 SMUTC-PD's photo-response bandwidth and parasitic capacitance with different doping concentrations in the p-doped absorption region

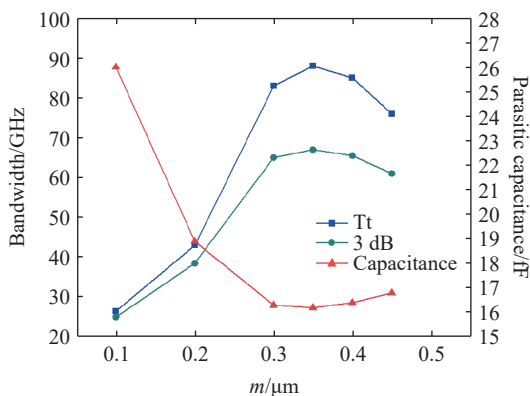


Fig. 7 SMUTC-PD's photo-response bandwidth and parasitic capacitance with different thicknesses of the p-doped absorption region

Next, the effect of electron transit in SMUTC-PD's collector layer on the PD's parasitic capacitance was analyzed. According to Ref. [17-18], this electron's transit velocity determined capacitance can be expressed by the following equation:

$$c = -\frac{dQ}{dv} = -i \frac{d\tau}{dV} = rP \frac{dv}{v^2 dE}, \quad (1)$$

where  $dQ$  is the change in electric charge for a given change in voltage,  $dV$ . It was concluded that this capacitance depends on the differentiation of the electron transit velocity with respect to the electric field intensity determining it, i.e., the curve slope of the electron transit velocity versus the electric field intensity. It can further reduce the SMUTC-PD's parasitic capacitance while the electron transits around its peak drift velocity. Finally, Fig. 8 (color online) depicts the frequency response of the optimized SMUTC-PD and of a MUTC-PD with the same structure except for the EFRL. The results show that the SMUTC-PD obtains a 3-dB bandwidth of 68 GHz, which is far greater than the MUTC-PD's 54 GHz 3-dB bandwidth, while the incident optical power is set to 1 mW only. According to Ref. [17], for a standard MUTC-PD, large incident optical power is needed to regulate the electric field intensity in the collector layer to obtain its electron's peak drift velocity. Thus, the proposed SMUTC-PD overcomes such limitations.

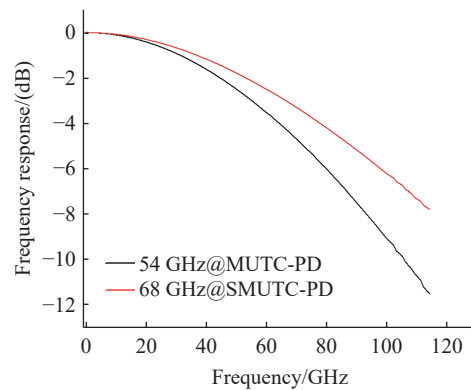


Fig. 8 SMUTC-PD's frequency response

According to [19], the reflectivity of the top electrode is set at 0.6. As shown in Fig. 9, the responsivity of SMUTC-PD is  $0.502 \text{ A/W}$ , while the

thickness of the absorption layer is set at 0.45  $\mu\text{m}$ .

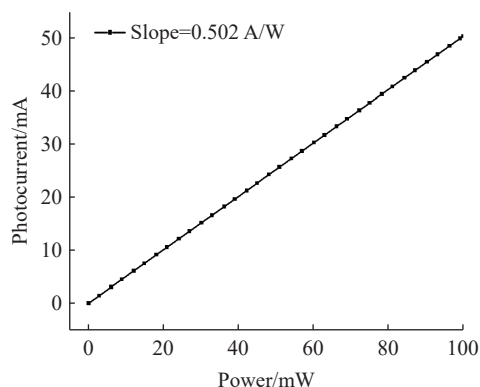


Fig. 9 SMUTC-PD's responsivity

## 4 Conclusion

In conclusion, this paper proposes a novel SMUTC-PD for 100 Gbit/s optical receivers. The electric field intensity in the collector layer is optimized by introducing an electric field regulation layer

after the cliff layer, ensuring that electrons consistently operate at peak velocity to offset the increased electron transit time caused by the extended collector layer while also achieving reduced capacitance. Additionally, this layer can redistribute the voltage between the absorption and collector layers, further enhancing the device's overall performance. Moreover, the device exhibits robust performance under low-power conditions, independent of incident optical power fluctuations. Ultimately, an optimal 3-dB bandwidth of 68 GHz with a responsivity of 0.502 A/W was attained, marking a significant 25.9% bandwidth enhancement compared to the original MUTC-PD's 54 GHz bandwidth. These findings demonstrate that the SMUTC-PD, featuring an electric field regulation layer, can effectively enhance the photodetector's high-speed performance, offering a promising solution for improving device bandwidth.

## References:

- [1] PAOLUCCI F, SGAMBELLURI A, EMMERICH R, *et al.*. Openconfig control of 100G/400G filterless metro networks with configurable modulation format and FEC[C]. *2019 Optical Fiber Communications Conference and Exhibition (OFC)*, IEEE, 2019: 1-3, doi: [10.1364/OFC.2019.Tu3H.4](https://doi.org/10.1364/OFC.2019.Tu3H.4).
- [2] ZHANG K R, HUANG Y Q, DUAN X F. Design and analysis of hybrid integrated high-speed mushroom vertical PIN photodetector[J]. *Applied Mechanics and Materials*, 2013, 411-414: 1455-1458.
- [3] EFFENBERGER F J, JOSHI A M. Ultrafast, dual-depletion region, InGaAs/InP p-i-n detector[J]. *Journal of Lightwave Technology*, 1996, 14(8): 1859-1864.
- [4] KATO K, HATA S, KAWANO K, *et al.*. Design of ultrawide-band, high-sensitivity p-i-n photodetectors[J]. *IEICE Transactions on Electronics*, 1993, E76-C(2): 214-221.
- [5] LI X, DEMIGUEL S, LI N, *et al.*. Backside illuminated high saturation current partially depleted absorber photodetectors[J]. *Electronics Letters*, 2003, 39(20): 1466-1467.
- [6] ISHIBASHI T, ITO H. Uni-traveling-carrier photodiodes[J]. *Journal of Applied Physics*, 2020, 127(3): 031101.
- [7] LI Q L, LI K J, FU Y, *et al.*. High-power flip-chip bonded photodiode with 110 GHz bandwidth[J]. *Journal of Lightwave Technology*, 2016, 34(9): 2139-2144.
- [8] SRIVASTAVA S. *Simulation study of InP-based uni-traveling carrier photodiode*[D]. Cincinnati: University of Cincinnati, 2003.
- [9] LI J, XIONG B, LUO Y, *et al.*. Ultrafast dual-drifting layer uni-traveling carrier photodiode with high saturation current[J]. *Optics Express*, 2016, 24(8): 8420-8428.
- [10] CHAO E F, XIONG B, SUN CH ZH, *et al.*. D-band MUTC photodiodes with flat frequency response[J]. *IEEE Journal of Selected Topics in Quantum Electronics*, 2022, 28(2): 3802208.
- [11] ZHEN ZH, HAO R, XING D, *et al.*. Nearly-ballistic optimization design of high-speed uni-traveling-carrier photodiodes[J]. *Chinese Journal of Lasers*, 2020, 47(10): 1006003. (in Chinese).
- [12] ADACHI S. *Physical Properties of III-V Semiconductor Compounds*[M]. New York: John Wiley & Sons, 1992.
- [13] SHRESTHA Y R. *Numerical simulation of GaAsSb/InP uni-traveling carrier photodiode*[D]. Cincinnati: University of

- Cincinnati, 2005.
- [14] ISHIBASHI T, FURUTA T, FUSHIMI H, *et al.*. InP/InGaAs uni-traveling-carrier photodiodes[J]. *IEICE Transactions on Electronics*, 2000, E83-C(6): 938-949.
  - [15] FRIESE S. *Atlas.ti 8 Mac-user Manual Updated for Program Version 8.4*[M]. Berlin: ATLAS.ti, 2019.
  - [16] ZHANG P, ZHANG X P, ZHANG R. Design of broadband and high-output power uni-traveling-carrier photodiodes[J]. *Optics Communications*, 2016, 365: 194-207.
  - [17] ZHOU G, RUNGE P. Nonlinearities of high-speed p-i-n photodiodes and MUTC photodiodes[J]. *IEEE Transactions on Microwave Theory and Techniques*, 2017, 65(6): 2063-2072.
  - [18] DONG X W, LIU K, HUANG Y Q, *et al.*. Design of high-speed UTC-PD with optimization of its electron transit performance and parasitic capacitance[J]. *IEEE Photonics Journal*, 2023, 15(1): 1-9.
  - [19] SAKAI K, ISHIMURA E, NAKAJI M, *et al.*. High-current back-illuminated partially depleted-absorber p-i-n photodiode with depleted nonabsorbing region[J]. *IEEE Transactions on Microwave Theory and Techniques*, 2010, 58(11): 3154-3160.

#### Author Biographies:



LIU Kai (1972—), male, from Beijing, doctoral supervisor, received a bachelor's degree in applied electronic technology and a Ph.D. in fiber optic communications and optoelectronics from the Beijing University of Posts and Telecommunications (BUPT), China, in 1994 and 1999, respectively. He wrote a postdoctoral project on the research of optical pumped 1.3  $\mu\text{m}$  VCSEL at the University of Southern California, Los Angeles, CA, USA, in 2000 and 2001. He is an Associate Professor at the School of Electrical Engineering, BUPT. He is the author of more than twenty refereed journal articles and conference papers on optoelectronic technology. His research interests include optical interconnects, optoelectronics integration, and photonic devices for optical fiber communications. He has recently contributed to the single-mode VCSEL for optical interconnects and high-speed, high-power UTC-PD for radio on fiber systems. E-mail: [kliu@bupt.edu.cn](mailto:kliu@bupt.edu.cn)